JOURNAL OF SPACECRAFT AND ROCKETS
Vol. 40, No. 1, January–February 2003

Navier–Stokes Computations for Body/Cruciform Grid Fin Configuration

Herng Lin* and Juan Cheng Huang†
Chung Shan Institute of Science and Technology, Lung-Tan 325, Taiwan, Republic of China
and
Ching-Chang Chieng‡
National Tsing Hua University, Hsinchu 300, Taiwan, Republic of China

A grid fin is an unconventional aerodynamic lifting and control device consisting of an outer frame with internal grid framework of small chord. The present study performs the Navier–Stokes computations of turbulent flows past 1) a grid fin alone and 2) fin/body combination shapes at Mach numbers of 2.5 and 0.7. This work designs a procedure to generate a structure grid with a simple and efficient algorithm combining "block-off" and "multiblock" methods for the complex configurations. Full Navier–Stokes equations with a pointwise version of the Baldwin–Barth one-equation turbulence model are discretized into finite difference form and solved by an algorithm in a fully coupled, implicit, and large block structure, and the solution algorithm achieves satisfactory convergence. The comparisons between computations and experimental data are made, and the detailed flow structure near grid fins can be obtained and examined.

Nomenclature

$\hat{A}^{\pm}, \hat{B}^{\pm}, \hat{C}^{\pm}$	=	positive and negative splitting Jacobian matrices in the ξ, η, and ς directions.
C_A	=	axial-force coefficient of single fin
C_{BM}	=	bending-moment coefficient of single fin
C_{HM}	=	hinge-moment coefficient of single fin
C_Z	=	normal-force coefficient of single fin
$C_{\epsilon 1}, C_{\epsilon 2}$	=	empirical constants in the turbulence model
$\hat{D}$	=	source term Jacobian matrix
E_t	=	total energy
$\hat{\boldsymbol{E}}, \hat{\boldsymbol{F}}, \hat{\boldsymbol{G}}$	=	inviscid flux vectors in transformed coordinates
$\hat{\boldsymbol{E}}_v, \hat{\boldsymbol{F}}_v, \hat{\boldsymbol{G}}_v$	=	viscous flux vectors in transformed coordinates
f_2, f_μ	=	damping function for pointwise version of Baldwin–Barth one-equation model
$\hat{\boldsymbol{H}}$	=	flux vectors of source term in transformed coordinates
J	=	Jacobian
$\boldsymbol{P}$	=	production term of turbulent kinetic energy per unit mass
p	=	static pressure
$\hat{\boldsymbol{Q}}$	=	vector of dependent variables
R_T	=	turbulent Reynolds number
$\hat{R}, \hat{R}^{-1}$	=	right-eigenvector matrix of flux Jacobian and its inverse matrix
$\Re$	=	turbulent variable for pointwise version of Baldwin–Barth one-equation model
t	=	dimensionless time, L/C_∞, L: characteristic length, C_∞: freestream soundspeed
U	=	contravariant velocity in the ξ directions
u	=	velocity component in the x direction of Cartesian coordinate
V	=	contravariant velocity in the η directions
v	=	velocity component in the y direction of Cartesian coordinate
W	=	contravariant velocity in the ς directions
w	=	velocity component in the z direction of Cartesian coordinate
x, y, z	=	three directions of Cartesian coordinates
Ycp	=	Y location of aerodynamic center
ε	=	dissipation rate of turbulent kinetic energy κ
κ	=	turbulent kinetic energy
$\hat{\lambda}^l$	=	eigenvalues of flux Jacobians
μ_{eff}	=	effective viscosity, which is equal to the summation of μ_t and μ_l
μ_l	=	molecular viscosity
μ_t	=	turbulent viscosity
ξ, η, ς	=	three directions of transformed coordinates
ρ	=	density
σ	=	empirical constants in the turbulence model

Received 6 December 2001; revision received 18 June 2002; presented as Paper 2002-2722 at the AIAA 20th Applied Aerodynamics Conference, St. Louis, MO, 24–26 June 2002; accepted for publication 13 August 2002.

*Scientist, P.O.X. 90008-15-5.
†Associate Scientist, P.O.X. 90008-15-5.
‡Professor, Department of Engineering and System Science. Associate Fellow AIAA.

Introduction

A GRID fin is an unconventional aerodynamic lifting and control device consisting of outer frames with internal grid frameworks of small chord (Fig. 1). Typical cross hatching of the fin divides it into squares and triangular segments as shown in Fig. 2. The small chord dimensions of the device result in small variations in positions of center of pressure and near-zero hinge moment over wide Mach-number range, so that the size of control actuator systems can be reduced. In addition, the grid fin design also leads to different stall characteristics from that of planar fins, especially at high angles of attack.

Aerodynamic characteristics of different grid fin configurations have been investigated by Washington and Miller,[1] such as the effects of internal grid framework, Mach number, angle of attack, and fin deflection angle on grid fin aerodynamics. Very small hinge moments caused by the grid fin and comparable magnitudes in normal force and the root bending moments caused by grid fins and planar fins of similar size have been observed. The reduction of grid-fin drag levels has been further studied[2] by six grid fin designs emphasizing the effects of outer frame cross section and web thickness for Mach numbers ranging from 0.5 to 2.5. Furthermore, subsonic/transonic free-flight tests of same body missiles with and without grid fins have been conducted[3] for Mach numbers ranging from 0.39 to 1.6 in the Aeroballistic Research Facility. The aerodynamic data also indicate that there are normal shocks existing inside the grid cells at some critical Mach number.

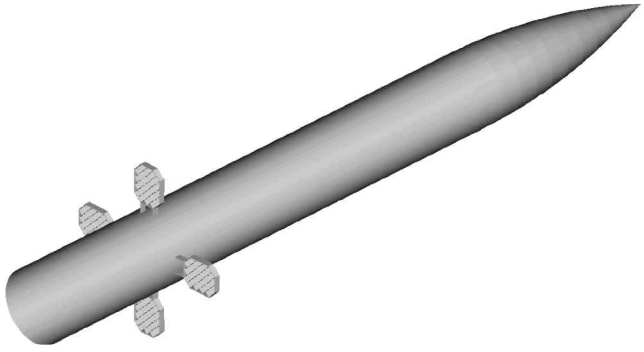

Fig. 1 Sketch of wind-tunnel testing model.

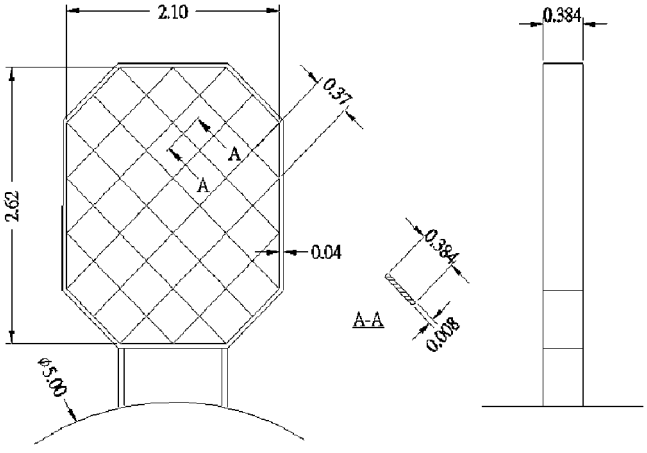

Fig. 2 Grid-fin frame cross section.

It is always interesting to predict the just-mentioned phenomena by analytical or numerical methods from fundamental conservation laws. A vortex lattice method has been the first intended to analyze the lift characteristics of grid fins for the subsonic regime,[4] and it can be extended for missiles at large angles of attack. Good agreements between experimental data and theoretical predictions have been obtained for the grid fins considered up to angles of attack about 45 deg. Starting from 1995, numerical simulations solving Euler equations[5] with computational meshes generated by ICEMCFD MULCAD software had been performed, so that the aerodynamic effect of the fairing ramp can be quantified. Until 2000, Navier–Stokes simulations[6,7] for the flow over missiles with grid fins were obtained by the commercial unstructured-grid solver (FLUENT) solving three-dimensional time-dependent Reynolds-averaged Navier–Stokes equations with the Spalart–Allmaras one-equation turbulence model. Second-order upwind discretization by Roe's method was used for the flow variables and turbulent viscosity equation. Spalart–Allmaras model with wall function was applied to resolve the effect caused by inefficient fine mesh near–wall region. The computations were made at a Mach number of 2.5 and several angles of attack for a missile without fins, with planar fins, and with grid fins. Good agreement with the measured data was obtained for all configurations investigated.

For efficient computational work the grid-generation method and the efficient solver are the base elements. The present study adopts a structured grid system instead of an unstructured grid system so that more flexible choices of the existing solution algorithms can be made. It means a simple but efficient grid-generation algorithm must be designed to eliminate the grid-generation work, especially for complex flow configurations. Present work extended the blocking-off concept introduced by Patankar[8] in incompressible flow computation. In Patankar's approach a rectangular grid can be modified to handle an irregular-shaped calculation domain by blocking off part of the control volume for the desired irregular domain, that is, establishing known values of the relevant flow variables in the inactive control volumes. Employing the "block-off" grid concept, the solid region is also included in the solution domain and acts a part of the grid system. For example, if the inactive region represented a stationary solid boundary the velocity component in this region must be set equal to zero. The similar concept, the fortified Navier–Stokes concept,[9] was employed to handle complex body configurations and improve local grid resolution. The present algorithm solves the full Navier–Stokes equations with a pointwise version of the Baldwin–Barth one-equation turbulence model in a fully coupled, implicit, and large block structure. Numerical schemes solving flow variables in delta form are described in the following sections.

Governing Equations

The differential equations describing the flow for this study are the three-dimensional, time-dependent, compressible, mass-averaged Navier–Stokes equations with the one-equation turbulence model of pointwise version of the Baldwin–Barth model.[10] The resulting nondimensional equations in conservation law form can be formulated in the curvilinear coordinates as follows:

$$\frac{\partial \hat{\boldsymbol{Q}}}{\partial t}+\frac{\partial \hat{\boldsymbol{E}}}{\partial \xi}+\frac{\partial \hat{\boldsymbol{F}}}{\partial \eta}+\frac{\partial \hat{\boldsymbol{G}}}{\partial \varsigma}=\frac{\partial \hat{\boldsymbol{E}}_v}{\partial \xi}+\frac{\partial \hat{\boldsymbol{F}}_v}{\partial \eta}+\frac{\partial \hat{\boldsymbol{G}}_v}{\partial \varsigma}+\hat{\boldsymbol{H}} \tag{1}$$

where $\hat{\boldsymbol{Q}}, \hat{\boldsymbol{E}}, \hat{\boldsymbol{F}}, \hat{\boldsymbol{G}}, \hat{\boldsymbol{E}}_v, \hat{\boldsymbol{F}}_v, \hat{\boldsymbol{G}}_v$ are 6×1 column matrices with the elements of

$$\hat{\boldsymbol{Q}}=\frac{1}{J}[\rho,\ \rho u,\ \rho v,\ \rho w,\ E_t,\ \Re], \qquad \hat{\boldsymbol{E}}=\frac{1}{J}\begin{bmatrix}\rho U\\ \rho uU+\xi_x p\\ \rho vU+\xi_y p\\ \rho wU+\xi_z p\\ U(E_t+p)\\ \Re U\end{bmatrix}$$

$$\hat{\boldsymbol{F}}=\frac{1}{J}\begin{bmatrix}\rho V\\ \rho uV+\eta_x p\\ \rho vV+\eta_y p\\ \rho wV+\eta_z p\\ V(E_t+p)\\ \Re V\end{bmatrix}, \qquad \hat{\boldsymbol{G}}=\frac{1}{J}\begin{bmatrix}\rho W\\ \rho uW+\varsigma_x p\\ \rho vW+\varsigma_y p\\ \rho wW+\varsigma_z p\\ W(E_t+p)\\ \Re W\end{bmatrix}$$

$$\hat{\boldsymbol{E}}_v=\frac{1}{\mathrm{Re}_\infty J}\begin{bmatrix}0\\ \tau_{xx}\xi_x+\tau_{xy}\xi_y+\tau_{xz}\xi_z\\ \tau_{xy}\xi_x+\tau_{yy}\xi_y+\tau_{yz}\xi_z\\ \tau_{xz}\xi_x+\tau_{yz}\xi_y+\tau_{zz}\xi_z\\ E_{v5}\\ \dfrac{-\mu_t}{\rho\sigma_\varepsilon}(\xi_x\Re_x+\xi_y\Re_y+\xi_z\Re_z)\end{bmatrix}$$

$$\hat{\boldsymbol{F}}_v=\frac{1}{\mathrm{Re}_\infty J}\begin{bmatrix}0\\ \tau_{xx}\eta_x+\tau_{xy}\eta_y+\tau_{xz}\eta_z\\ \tau_{xy}\eta_x+\tau_{yy}\eta_y+\tau_{yz}\eta_z\\ \tau_{xz}\eta_x+\tau_{yz}\eta_y+\tau_{zz}\eta_z\\ E_{v5}\\ \dfrac{-\mu_t}{\rho\sigma_\varepsilon}(\eta_x\Re_x+\eta_y\Re_y+\eta_z\Re_z)\end{bmatrix}$$

$$\hat{\boldsymbol{G}}_v=\frac{1}{\mathrm{Re}_\infty J}\begin{bmatrix}0\\ \tau_{xx}\varsigma_x+\tau_{xy}\varsigma_y+\tau_{xz}\varsigma_z\\ \tau_{xy}\varsigma_x+\tau_{yy}\varsigma_y+\tau_{yz}\varsigma_z\\ \tau_{xz}\varsigma_x+\tau_{yz}\varsigma_y+\tau_{zz}\varsigma_z\\ E_{v5}\\ \dfrac{-\mu_t}{\rho\sigma_\varepsilon}(\varsigma_x\Re_x+\varsigma_y\Re_y+\varsigma_z\Re_z)\end{bmatrix}$$

$$\hat{\boldsymbol{H}}=\frac{1}{J}[0,\ 0,\ 0,\ 0,\ 0,\ H_6]^T$$

The elements in the matrices are

$$E_{v5} = u(\tau_{xx}\xi_x + \tau_{xy}\xi_y + \tau_{xz}\xi_z) + v(\tau_{xy}\xi_x + \tau_{yy}\xi_y + \tau_{yz}\xi_z) + w(\tau_{xz}\xi_x + \tau_{yz}\xi_y + \tau_{zz}\xi_z) + \dot{q}_x\xi_x + \dot{q}_y\xi_y + \dot{q}_z\xi_z$$

$$F_{v5} = u(\tau_{xx}\eta_x + \tau_{xy}\eta_y + \tau_{xz}\eta_z) + v(\tau_{xy}\eta_x + \tau_{yy}\eta_y + \tau_{yz}\eta_z) + w(\tau_{xz}\eta_x + \tau_{yz}\eta_y + \tau_{zz}\eta_z) + \dot{q}_x\eta_x + \dot{q}_y\eta_y + \dot{q}_z\eta_z$$

$$G_{v5} = u(\tau_{xx}\varsigma_x + \tau_{xy}\varsigma_y + \tau_{xz}\varsigma_z) + v(\tau_{xy}\varsigma_x + \tau_{yy}\varsigma_y + \tau_{yz}\varsigma_z) + w(\tau_{xz}\varsigma_x + \tau_{yz}\varsigma_y + \tau_{zz}\varsigma_z) + \dot{q}_x\varsigma_x + \dot{q}_y\varsigma_y + \dot{q}_z\varsigma_z$$

$$H_6 = (C_{\varepsilon 2}f_2 - C_{\varepsilon 1})(\Re \boldsymbol{P})^{\frac{1}{2}} + \left(\frac{1}{\mathrm{Re}_\infty J\rho}\right)\left(\mu_l + \frac{2\mu_t}{\sigma_\varepsilon}\right)\nabla^2\Re$$

$$J^{-1} = x_\xi y_\eta z_\varsigma + x_\varsigma y_\xi z_\eta + x_\eta y_\varsigma z_\xi - x_\xi y_\varsigma z_\eta - x_\varsigma y_\eta z_\xi - x_\eta y_\xi z_\varsigma$$

$$U = \xi_x u + \xi_y v + \xi_z w, \qquad V = \eta_x u + \eta_y v + \eta_z w$$

$$W = \varsigma_x u + \varsigma_y v + \varsigma_z w$$

$$\mu_{\mathrm{eff}} = \mu_l + \mu_t, \qquad \tau_{xx} = \frac{2}{3}\mu_{\mathrm{eff}}(2u_x - v_y - w_z)$$

$$\tau_{yy} = \frac{2}{3}\mu_{\mathrm{eff}}(2v_y - u_x - w_z), \qquad \tau_{zz} = \frac{2}{3}\mu_{\mathrm{eff}}(2w_z - u_x - v_y)$$

$$\tau_{xy} = \mu_{\mathrm{eff}}(u_y + v_x), \qquad \tau_{yz} = \mu_{\mathrm{eff}}(v_z + w_y)$$

$$\tau_{xz} = \mu_{\mathrm{eff}}(u_z + w_x), \qquad \dot{q}_x = \kappa(\xi_x T_\xi + \eta_x T_\eta + \varsigma_x T_\varsigma)$$

$$\dot{q}_y = \kappa(\xi_y T_\xi + \eta_y T_\eta + \varsigma_y T_\varsigma), \qquad \dot{q}_z = \kappa(\xi_z T_\xi + \eta_z T_\eta + \varsigma_z T_\varsigma)$$

$$\kappa = \frac{(\mu_l/Pr_l + \mu_t/Pr_t)}{\gamma - 1}$$

The variable $\Re$ for the turbulence model is defined as κ/ε^2. $\boldsymbol{P}$ is expressed as

$$\boldsymbol{P} = (\mu_t/\rho)\left[2\left(u_x^2 + v_y^2 + w_z^2\right) + (u_y + u_z + v_x + v_z + w_x + w_y)\right]$$

σ, $C_{\varepsilon 1}$, $C_{\varepsilon 2}$ are empirical constants in the turbulence model.[10] Effective viscosity μ_{eff} consists of two parts: turbulent viscosity μ_t and molecular viscosity μ_l. The turbulent viscosity is expressed as $\mu_t = C_\mu \rho f_\mu \Re$.

Numerical Algorithm

The finite volume approach is used for the formulations of difference equations. The fully implicit discrete form of Eq. (1) can be written in a delta form as follows:

$$\hat{\boldsymbol{Q}}^{n+1}_{i,j,k} - \hat{\boldsymbol{Q}}^{n}_{i,j,k} = (\mathrm{RHS})^{n+1}$$

$$\mathrm{RHS} = -(\Delta t/\Delta\xi)\left[(\bar{E} - \bar{E}_v)_{i+\frac{1}{2},j,k} - (\bar{E} - \bar{E}_v)_{i-\frac{1}{2},j,k}\right] - (\Delta t/\Delta\eta)\left[(\bar{F} - \bar{F}_v)_{i,j+\frac{1}{2},k} - (\bar{F} - \bar{F}_v)_{i,j-\frac{1}{2},k}\right] - (\Delta t/\Delta\varsigma)\left[(\bar{G} - \bar{G}_v)_{i,j,k+\frac{1}{2}} - (\bar{G} - \bar{G}_v)_{i,j,k-\frac{1}{2}}\right] + \Delta t\hat{H}_{i,j,k} \tag{2}$$

In this study central difference approximation is used for the viscous terms $\hat{\boldsymbol{E}}_v$, $\hat{\boldsymbol{F}}_v$, $\hat{\boldsymbol{G}}_v$, and the total-variation-diminishing numerical flux proposed by Yee and Harten[11] is applied for the convective terms $\hat{\boldsymbol{E}}$, $\hat{\boldsymbol{F}}$, and $\hat{\boldsymbol{G}}$.

In the present study the equation set is solved simultaneously using the implicit unfactored backward-Euler scheme[12] for time integration. After the upwind-differencing approximation in the ξ, η, and ς directions, the resulting difference equations for the full Navier–Stokes equations and the transport equation of variable $\Re$ can be written as[12]

$$\left[1 + \Delta t\left(\frac{\partial\hat{A}^+}{\partial\xi^-} + \frac{\partial\hat{A}^-}{\partial\xi^+} + \frac{\partial\hat{B}^+}{\partial\eta^-} + \frac{\partial\hat{B}^-}{\partial\eta^+} + \frac{\partial\hat{C}^+}{\partial\varsigma^-} + \frac{\partial\hat{C}^-}{\partial\varsigma^+} - \hat{D}\right)\right]^n \times \Delta Q^n_{i,j,k} = (\mathrm{RHS})^n \tag{3}$$

Where $\hat{A}^\pm$, $\hat{B}^\pm$, $\hat{C}^\pm$ are the positive and negative splitting Jacobian matrices in the ξ, η, and ς directions. Generally, the split Jacobian matrices $\hat{A}^\pm$, $\hat{B}^\pm$, $\hat{C}^\pm$ are modified to maintain the stability of the thin-layer viscous term. They are given as follows[13]:

$$\hat{A}^\pm = \hat{R}_\xi\left(\hat{\lambda}^\pm_\xi \pm \bar{\nu}_\xi I\right)\hat{R}^{-1}_\xi, \qquad \hat{B}^\pm = \hat{R}_\eta\left(\hat{\lambda}^\pm_\eta \pm \bar{\nu}_\eta I\right)\hat{R}^{-1}_\xi$$

$$\hat{C}^\pm = \hat{R}_\varsigma\left(\hat{\lambda}^\pm_\varsigma \pm \bar{\nu}_\varsigma I\right)\hat{R}^{-1}_\varsigma, \qquad \bar{\nu}_\xi = \frac{2\gamma M_\infty(\mu_{\mathrm{eff}}/\rho)|\Delta\xi|^2}{(\mathrm{Re}_\infty Pr)}$$

where $\hat{R}$, $\hat{R}^{-1}$ are the right-eigenvector matrix of flux Jacobian $\partial\hat{E}/\partial\hat{Q}$ and its inverse and $\hat{\lambda}^l s$ are the eigenvalues of flux Jacobians $\partial\hat{E}/\partial\hat{Q}$.

The source term $\hat{\boldsymbol{H}}$ can be very large and cause the equation to be set very stiff. To mitigate the stiff problem, the source terms are treated implicitly.[14] Employing the lower-diagonal-upper implicit (LDU)[15] scheme, Eq. (3) can be written in the following form:

$$(L + D + U)\Delta\hat{\boldsymbol{Q}}^n = -\Delta t(\mathrm{RHS})^n \tag{4}$$

The approximate factorization method factorizes the preceding equation into

$$(L + D)D^{-1}(D + U)\Delta\hat{\boldsymbol{Q}}^n = -\Delta t(\mathrm{RHS})^n \tag{5}$$

So Eq. (5) can be solved in three steps. Finally, the primitive conservation variables on time level $n+1$ can be obtained by $\hat{\boldsymbol{Q}}^{n+1} = \hat{\boldsymbol{Q}}^n + \Delta Q^n$. In addition to the preceding schemes, the space-varying time step[16] for cell (i, j, k) is employed, that is,

$$(\Delta t)_{i,j,k} = (\Delta t)_{\mathrm{ref}}\Big/\left(1 + \sqrt{J}\right)$$

Grid-Generation Procedure

Figure 1 shows the sketch of the wind-tunnel testing model[2] under present investigation; it is a 10.4-caliber, four-grid-fin (cruciform) missile shape. The missile has a three-calibers tangent-ogive nose, faired into a 7.4-caliber afterbody. These four-fin hinge axes are located 2.0 calibers before the end of the missile. The body diameter is 5 in. The chord length of grid fin is of 0.384 in. with web thickness of 0.008 in. The internal arrangement of grid is of a cross-honeycomb type (Fig. 2). The frame cross section is rectangular such that the thickness is constant from leading to trailing edge. The thickness of outer shell is simplified as 0.04 in. (The dimension of the outer shell for the test model[2] is varied from 0.02 to 0.06 in.) Two rectangular plates of thickness 0.04 in. act as the support structure simply connected to the missile body. The distance, where the fin is offset from the body centerline, is 0.598 in.

In the present study the multiblock grid and block-off-type grid treatments are combined. The procedure generating the entire grid system consists of six steps and will be described first in the following paragraphs:

At first, a base grid is generated for a single fin (or fin alone), and the fin is of complex structure like as honeycomb. The grid fin is composed of basic elements with cross sections as equal-side right triangles plus a slit web (Fig. 3). A transfinite interpolation scheme[17] is employed to generate the grid points on lines describing the slit web (BE and AF) and the interior grid points (the triangle BDE) after specific auxiliary points C and G on the line segments BD and BE are chosen. The triangle ADF has a right angle at point D, and

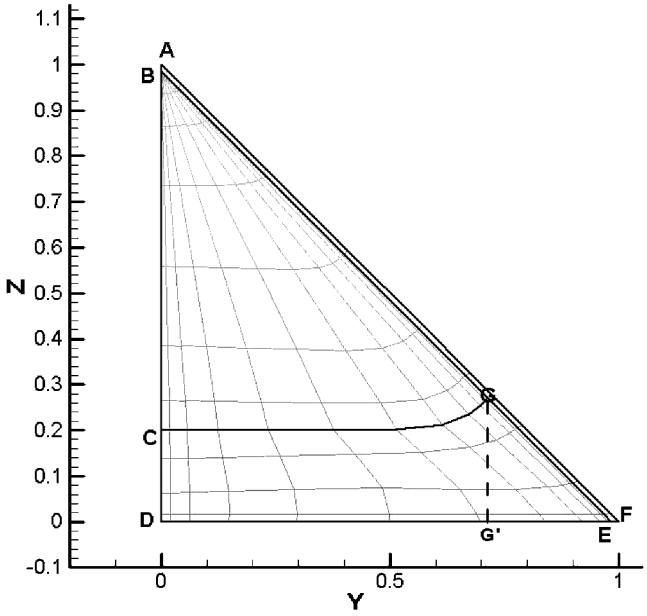

Fig. 3 Basic two-dimensional grid on y–z coordinate plane for equal-side triangular element.

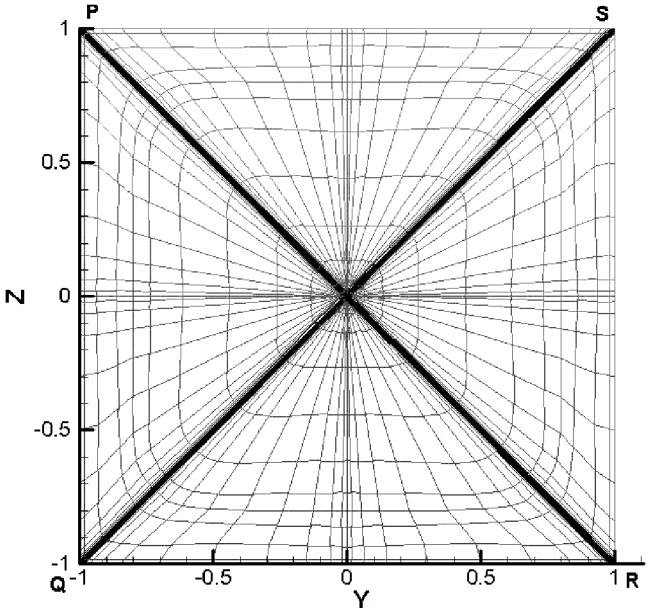

Fig. 4 Basic two-dimensional grid on y–z coordinate plane for square element.

the sides DA and DF are of the same length. The unit length for sides DA and DF in Fig. 3 are equal to 0.2625 in. The slit region ABEF represents a half of the web, that is, the distance of the parallel line segments AF and BE must be set to half-thickness of the web. The auxiliary points C and G are chosen with the height in the Z direction of point G greater than the height of point C (i.e., GG′ > CD), so that the auxiliary curve CG is orthogonal to the line BE. Other grid points on region BCG and region CDEG boundaries are distributed on line segments BC, BG, CD, DE, EG, and curve CG. Figure 3 shows the good grid quality in terms of the grid point distribution and orthogonal property. Three grid systems consisting of 11×11, 13×13, 15×15, and 17×17 points in the Y and Z directions are obtained, and the grid-refinement test proves that a 11×11 grid point of a basic element is fine enough.

Second, the grid node distribution of basic element ADE is repeated to construct a square element PQRS with a pair of X-type webs in Fig. 4; therefore, Fig. 3 is $\frac{1}{8}$ of Fig. 4. For the two-dimensional square element PQRS the periodic boundary condition is applied on the line segment OR (O is the center point), where two grid lines are overlapped. The black-band region in Fig. 4 consists of three lines that represent the web solid structure and is treated as the block-off grid region.

Third, the main frame of the Y–Z cross section for the entire grid fin is obtained by repeating the square element PQRS or the triangular base element ADF, that is, Figs. 3 and 4 are used repeatedly to generate Fig. 5 and so on. Then block-1 to block-20 are generated to form the grid for a single grid fin in two dimensions (two-dimensional grid). Hyperbolic grid generation is performed in the outside region of the grid fin, and the gridlines start from the boundary grids of the grid fin. The far extensions from the gridlines are made to avoid the incorrect wave reflections, as shown from the block-25 to block-28 grid.

In the last step extending the two-dimensional grid (Fig. 5, block 1 to block 28) in the X direction so that the three-dimensional multi-block grid system for grid fin alone is completed (Fig. 6). The block-interface, symmetric line, wall, far-field boundary conditions and block-off grid region must be specified and configured in the entire grid system.

One or one-plus-two-half grid system of a single grid fin in Fig. 5 can be connected to the missile body and form a horizontal-fin/body

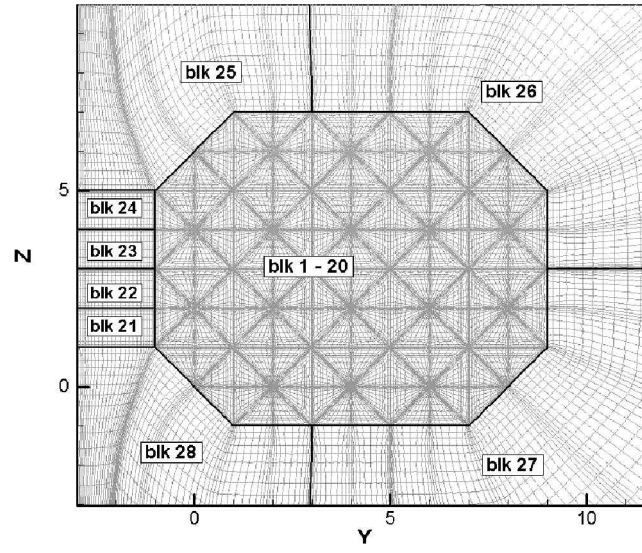

Fig. 5 Two-dimensional grid for Y–Z cross section for grid-fin-alone grid systems.

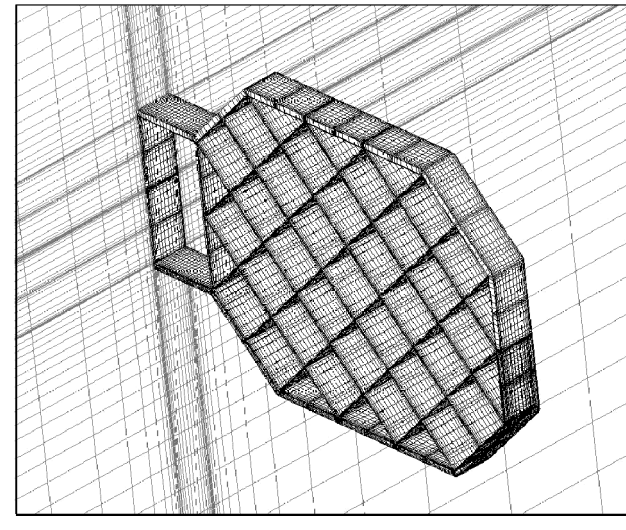

Fig. 6 Three-dimensional multiblock grid system for grid-fin-alone computation.

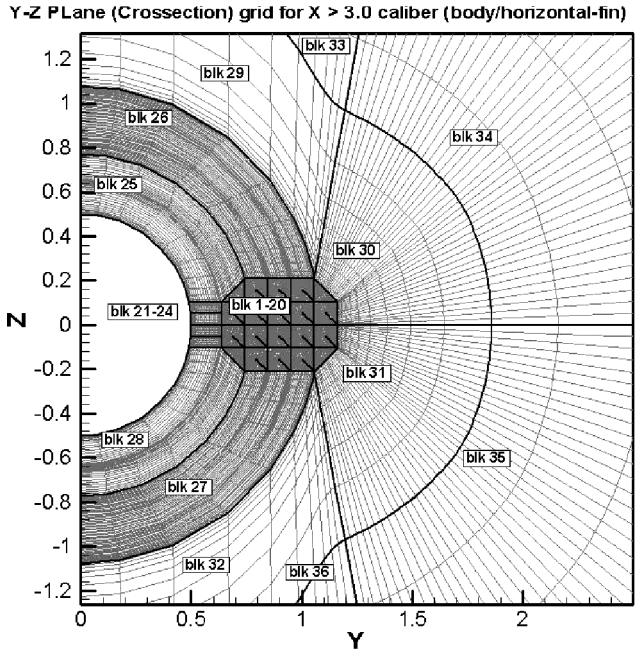

Fig. 7 Two-dimensional grid for Y–Z cross section for body/horizontal-fin configuration grid systems (near grid fin, 36 blocks).

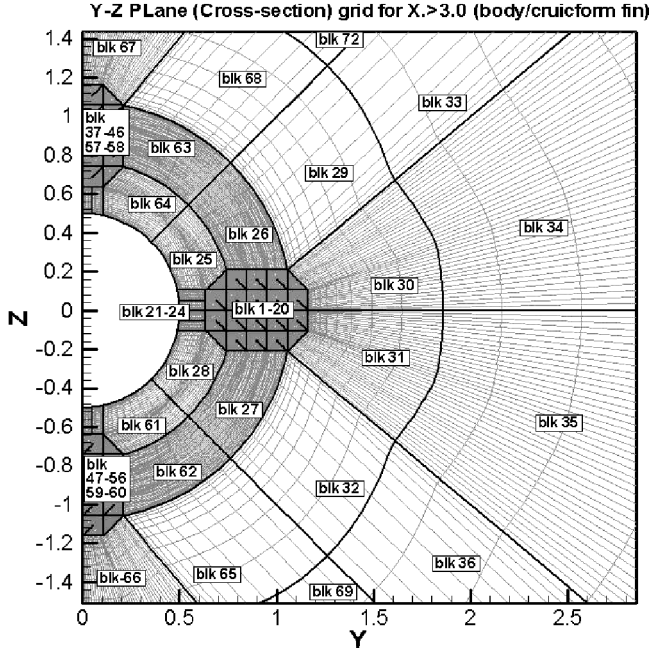

Fig. 8 Two-dimensional grid for Y–Z cross section for body/cruciform fin configuration grid systems (near grid fin, 72 blocks).

shape grid (36 blocks as shown in Fig. 7) or a cruciform-fin/body shape grid (72 blocks as shown in Fig. 8). The H-O-type topologies are adopted for the flowfield grid around the fin-body shape. The flow regime at the base region is not the emphasis in the present study; therefore, the extended-body-type grid is adopted in the x direction. The completed three-dimensional grid distributions for cruciform-fin/body configuration are plotted in Fig. 9.

Block-Off-Type Grid Region Treatment

For all grids containing solid structure the block-off-type grid is adapted, and the basic procedure for the treatment is described as follows. First, generate an H-type mesh on the solid-body region (inactive region). Second, apply no-slip boundary treatment to evaluate numerical flux and flow variables on the solid-body surface. Third, add a great value (for example, 10^{29}) to diagonal elements of the matrix D of Eq. (5) to ensure the system equations with the diagonal-

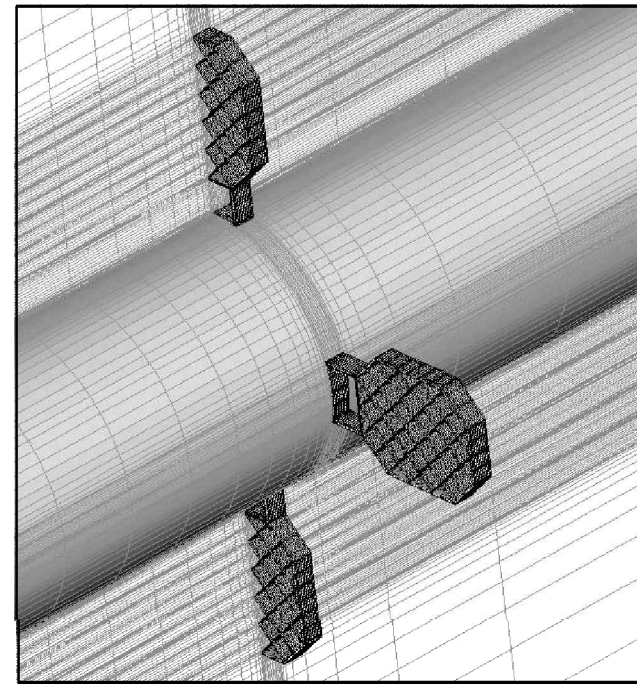

Fig. 9 Three-dimensional multiblock grid system for body/cruciform-fin configuration.

dominate property. The treatment enforces the conservative-variable increment $\Delta\hat{Q}$ to equal zero in the block-off grid region after each iteration step. Fourth, carefully specify the conservation variables in the block-off grid region to avoid incorrect cell-interface numerical flux evaluation. In the present study density and static pressure in this region are set as twice of total density and total pressure, velocity components are set to zero, and the turbulent variable $\Re$ is set to a small value as 10^{-5}.

Results and Discussion

The grid-independent tests for grid-fin-alone configuration are carried out for Mach number 2.5 with freestream chord Reynolds number 5×10^6 at 5- and 15-deg angles of attack. The grid-fin frame cross-section shape is shown in Fig. 2 with a reduced chord length of 0.2625 in. Two classes of grid systems are designed with different distributions near the wall region, that is, "fine-wall" and "coarse-wall" grid systems, so that the requirement of the resolution of grid point near the wall can be shown. Fine-wall or coarse-wall grid systems are named after the first grid line at a distance 0.0002 or 0.005 chord length off the web surface, respectively. The grid systems are constructed by basic equilateral right-angle triangular element with the points 11×11, 13×13, 15×15, 17×17 in the Y and Z directions. Figure 10 plots the convergence histories of the five grid-independent test cases (grid-fin-alone configuration) and one planar-form fin/body shape case. The L_2 residual of flow variables for these calculations can be four orders lower within 5000 ~ 6000 iterations, respectively; thus, the converged flow structure are achieved. The computed aerodynamic coefficients of normal force, axial force, hinge moment, and bending moment for fin alone are tabulated in Table 1. The computed aerodynamic coefficients for five-deg angle of attack of normal force, axial force, hinge moment, and bending moment for fin alone are tabulated in Table 1. It is observed that the discrepancies of computed aerodynamic coefficients from the fine-wall grid and coarse-wall grid computations are insignificant, although the fine-grid system might derive different distributions for eddy viscosity or local velocity profile near the wall of the web surface. The computed values of normal-force and bending-moment coefficients are exceedingly close for all grid systems, ranging from 11×11 to 17×17 points with fine-wall or coarse-wall refinements. And the computed axial-force and hinge-moment coefficients are very close by employing the grid points 13×13, 15×15, 17×17 in the Y and Z directions also. However, there is approximately a 7% difference in axial-force coefficients and a 3% difference in

Table 1 Computed aerodynamic coefficients using different grids for Mach number of 2.5 and 5-deg angle of attack ($M_\infty = 2.5, \alpha = 5, Re = 5 \times 10^6$)

Grid type[a]	Grid points (million)	Axial-force coefficient C_A	Normal-force coefficient C_Z	Bending-moment coefficient C_{bm}	Hinge-moment coefficient C_{hm}
F11 × 11	1.20	0.5017*E*+01	0.9711*E*+01	6.3788*E*+01	−4.9843*E*+00
C11 × 11	1.20	0.5032*E*+01	0.9682*E*+01	6.3600*E*+01	−4.9627*E*+00
F13 × 13	1.57	0.4656*E*+01	0.9733*E*+01	6.4006*E*+01	−5.1655*E*+00
C13 × 13	1.58	0.4672*E*+01	0.9696*E*+01	6.3767*E*+01	−5.1360*E*+00
F15 × 15	2.00	0.4661*E*+01	0.9779*E*+01	6.4328*E*+01	−5.1990*E*+00
C15 × 15	2.00	0.4675*E*+01	0.9738*E*+01	6.4066*E*+01	−5.1669*E*+00
F17 × 17	2.48	0.4547*E*+01	0.9798*E*+01	6.4479*E*+01	−5.2565*E*+00

[a]F = fine grid; C = coarse grid.

Table 2 Computed aerodynamic coefficients for different grids at Mach number of 2.5 and 15-deg angle of attack ($M_\infty = 2.5, \alpha = 15$ deg, $Re = 5 \times 10^6$)

Grid type[a]	No. of grid points (million)	Axial-force coefficient C_A	Normal-force coefficient C_Z	Bending-moment coefficient C_{bm}	Hinge-moment coefficient C_{hm}
F11 × 11	1.20	0.6387*E*+01	0.3266*E*+02	0.2165*E*+03	−0.1610*E*+02
F13 × 13	1.57	0.6002*E*+01	0.3288*E*+02	0.2182*E*+03	−0.1669*E*+02
F15 × 15	2.00	0.6014*E*+01	0.3306*E*+02	0.2194*E*+03	−0.1679*E*+02
F17 × 17	2.48	0.5979*E*+01	0.3312*E*+02	0.2202*E*+03	−0.1693*E*+02

[a]F = fine grid; C = coarse grid.

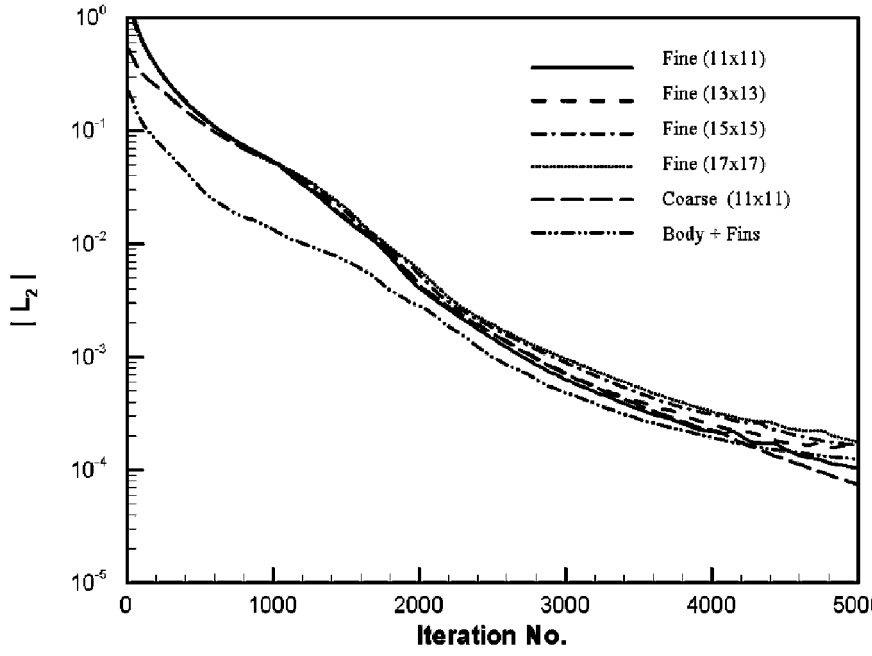

Fig. 10 Convergent histories for the cases of grid-fin-alone configurations; Mach number 2.5 and 5-deg angle of attack.

hinge-moment coefficients between the values using 11 × 11 or 13 × 13 grid system. The observations reveal that although the detailed turbulent flow physics can be questionable if only 4–7 or 2–3 points inside the boundary layer for fine-wall or coarse-wall grid systems exist for an unit grid cell, integrated variables as aerodynamic coefficients are still acceptable because of their values of small discrepancies. The computed aerodynamic coefficients for a 15-deg angle of attack of normal force, axial force, hinge moment, and bending moment for fin alone are tabulated in Table 2. The results are similar to results in Table 1. To save computational resources, the grid system consisting of 11 × 11 points in the Y and Z directions for one equilateral right-angle triangular element and coarse-wall grid distance on the grid fin web surface are selected to generate the 36-blocks planar-form configuration grid system.

Extending the two-dimensional grid systems shown in Figs. 7 and 8 in the axial direction generates the horizontal fin/body grids. There are 77 total stations in axial direction, with 17 stations for horizontal grid fin; the total grid number is approximately 1.67 million.

The horizontal-grid-fin/body shape is the configuration of major interest in the present work because the fin aerodynamic experimental data are available.[2] The calculations are made for freestream Mach numbers of 0.7 and 2.5 with body-diameter-based Reynolds number of 5×10^6 at angles of attack 5, 10, 15, and 20. Figure 11 shows that the computed fin normal coefficients are in good agreement with the experimental data for an angle of attack below 15 deg but are different for the case of 20-deg for a Mach number of 0.7. The linear relation between the normal force and angle of attack is achieved if the angle of attack is less than 5 deg, and the nonlinear-lift or near-stall characteristic is related to the turbulence characteristics. For the case of Mach number 2.5, the computed fin normal coefficients are in good agreement with the experimental data for 5, 10, and 15 deg angles of attack.

Figure 12 indicates that the axial-force coefficient C_A predictions are in good agreement with experiment for the angle of attack less than 10 deg, but the computed C_A are underestimated for 10, 15, and 20 angles of attack for Mach number 0.7. However, the computed C_A is overestimated for a 15-deg angle of attack and Mach number of 2.5 (Fig. 13), but the prediction can be improved by finer grid (Table 1). The computed hinge-moment coefficients are in good agreement with the experimental data for angle of attack below 10 deg and

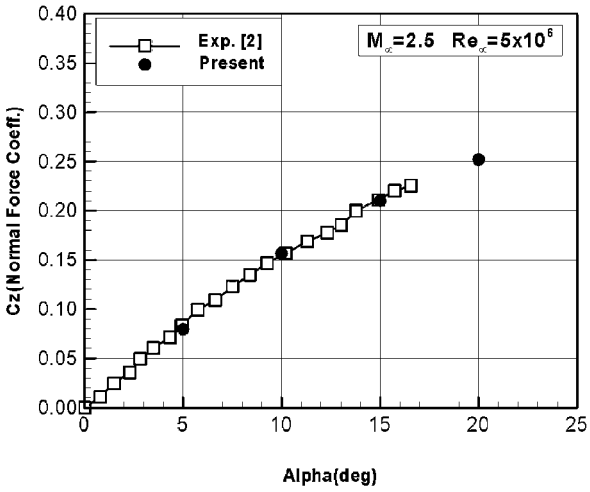

Fig. 11 Single-fin normal-force coefficients vs angle of attack (Mach number 2.5).

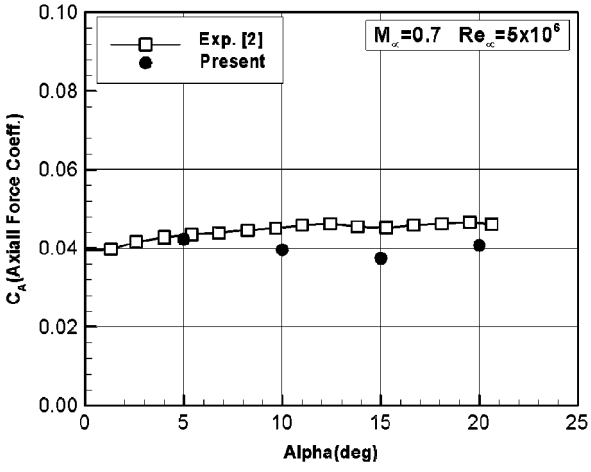

Fig. 12 Single-fin axial-force coefficients vs angle of attack (Mach number 0.7).

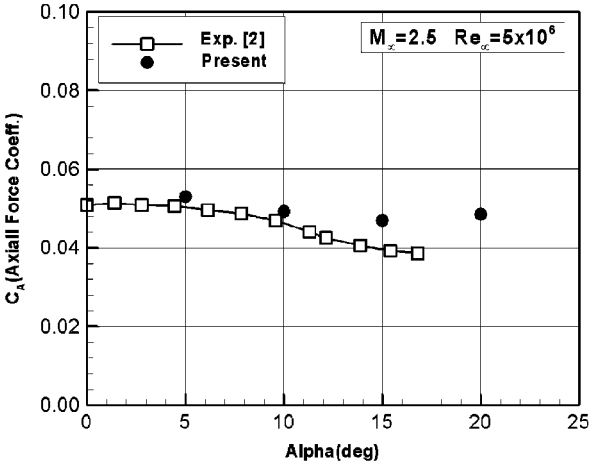

Fig. 13 Single-fin axial-force coefficients vs angle of attack (Mach number 2.5).

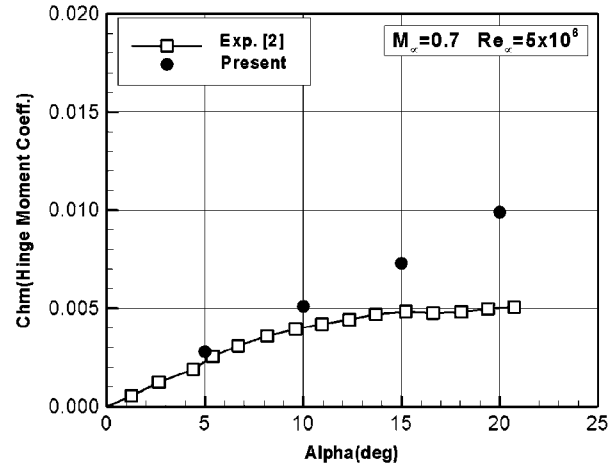

Fig. 14 Hinge-moment coefficients vs angle of attack (Mach number 0.7).

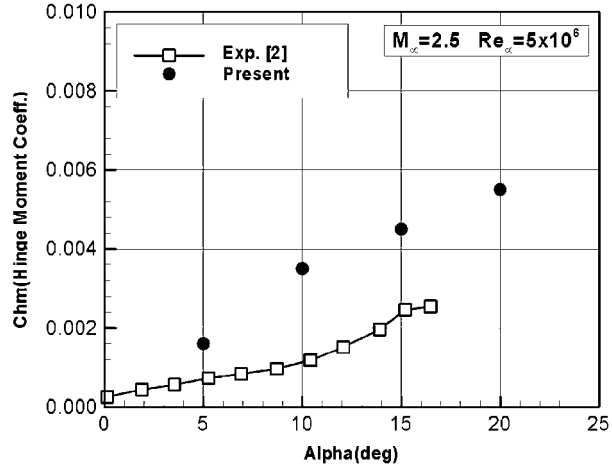

Fig. 15 Hinge-moment coefficients vs angle of attack (Mach number 2.5).

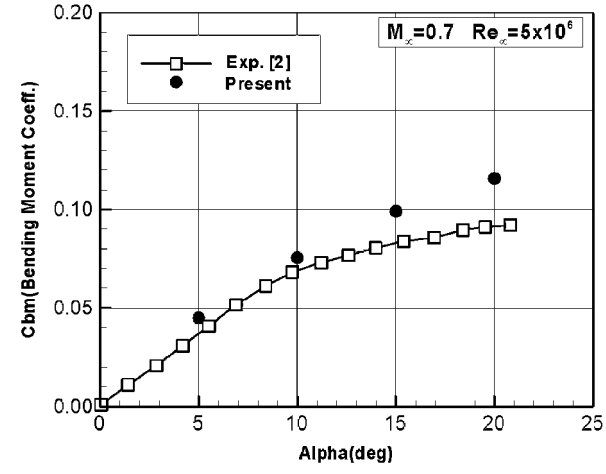

Fig. 16 Bending-moment coefficients vs angle of attack (Mach number 0.7).

are overestimated for the cases of 15 and 20 deg for Mach number 0.7 (Fig. 14). The overestimation is apparently enlarged for a Mach number of 2.5 (Fig. 15). This resulted from the overestimation of lift at the near-stall region. The x location of the aerodynamic center might be improved for finer grid point on axial distribution. Coarse grid distribution in the x direction will reduce the resolution of shock reflection and interaction and change the aerodynamic force distribution in each panel of the grid-fin frame. Figures 16 and 17 show that the computed bending-moment coefficients C_{BM} are in good agreement with experiments at angle of attack less than 10 deg for both Mach numbers. The trend is similar to those of Figs. 11 and 18. It indicates that a good prediction on the y value of aerodynamic center (Ycp) can be achieved.

Figure 19 plots the computed surface-pressure distributions on the grid fin for the flight condition of Mach number 2.5 and 20-deg angle of attack. There is a complex three-dimensional-shock structure

Table 3 Computed aerodynamic coefficients for flows over 1) planarform and 2) cruciform-fin/body combinations at freestream Mach number of 2.5 and 5-deg angle of attack

Grid-fin/body combination	Fin location	Axial-force coefficient C_A	Normal-force coefficient C_Z	Bending-moment coefficient C_{bm}	Hinge-moment coefficient C_{hm}
Cruciform type	Upper fin	4.502E−02	2.848E−02	0.000E+00	−2.014E−01
	Horizontal fin	4.641E−02	7.481E−02	6.495E−02	−6.383E−01
	Lower fin	4.816E−02	3.518E−02	0.000E+00	−3.379E−01
Planarform type	Horizontal fin	5.260E−02	7.966E−02	6.888E−02	−6.724E−01

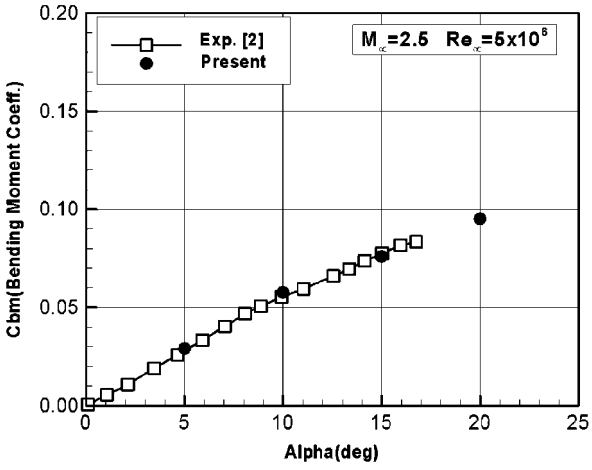

Fig. 17 Bending-moment coefficients vs angle of attack (Mach number 2.5).

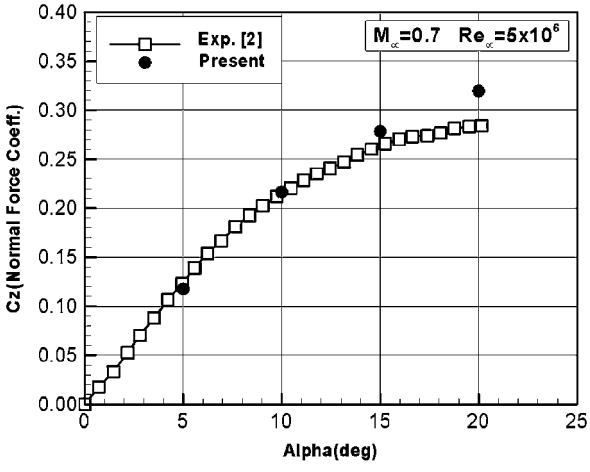

Fig. 18 Single-fin normal-force coefficients vs angle of attack (Mach number 0.7).

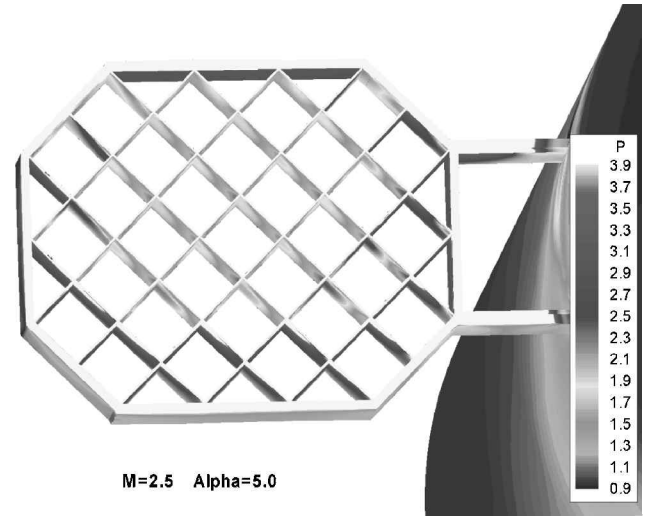

Fig. 19 Surface-pressure distributions of horizontal-fin/body configuration for the flight condition: Mach number 2.5 and 5-deg angle of attack (near grid fin).

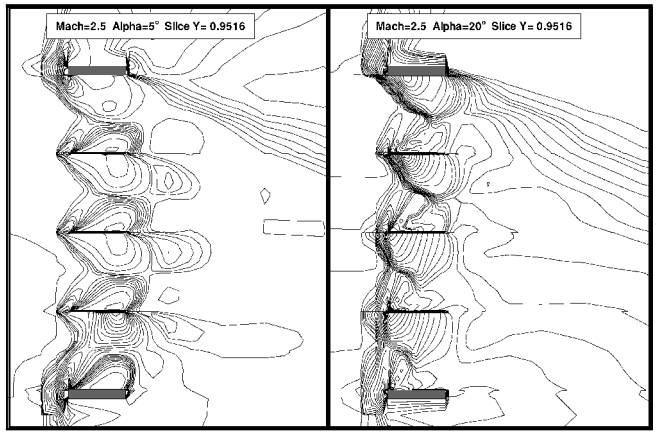

Fig. 20 Pressure distributions of the horizontal grid-fin X–Z cross section ($Y = 0.9516$ caliber), Mach number 2.5, 5- and 20-deg angle of attack.

emanating off the grid fins and exhibit high pressure at the region near-fin/body junctions. The high pressure on the top of the grid-fin frame reveals the generation of the pressure drag as a result of the configuration of outer frame apparently with the strong shock occurring at the surface facing the inflow.

Figure 20 plots the pressure contour on the X–Z cross-section plane (i.e., $Y = 0.9516$ caliber) of the horizontal fin for the cases of Mach number 2.5 at 5 and 20-deg angle of attack. Red bars in the figures indicate the solid region of the intersection of several webs and outer frame of the grid fin. For the case of 5-deg angle of attack shown in the left figure, the oblique shocks are attached in front of each web, and strong bow shock is occurred at the leading edge of outer frames. For the case of 20-deg angle of attack shown in the right figure, strong oblique shocks are occurred on the windside of each web and outer frames, but expansion wave are on the leeside.

Comparing the streamline patterns (Fig. 21) over the horizontal fin for Mach number 2.5 at 5 with 20-deg angle of attack reveals the existence of an apparent separated region for 20-deg angle of attack instead of smooth streamlines for a 5-deg angle of attack.

Figure 22 illustrates computed surface-pressure distributions on the cruciform-fins/body shape for the flight condition of Mach number 2.5 at a 5-deg angle of attack. The grid system is constructed using an equilateral right-angle triangular element with the 11 × 11 points of I and J directions, 72 blocks cruciform-fins/body shape grid system, 59 total stations in axial direction, 15 stations in the grid-fin chord, and a total of grid numbers of 2,580,000. The pressure distribution near the horizontal fin and fin/body junction is similar to Fig. 17. The details of aerodynamic coefficients for planar-form configuration are listed in Table 3 with the freestream Mach number 2.5 at 5-deg angle of attack. For the cruciform-fins/body shape the normal-force coefficient of horizontal fin is higher than the normal-force coefficients of upper and lower fin. Comparing the computed aerodynamic force and moment of horizontal fin for different

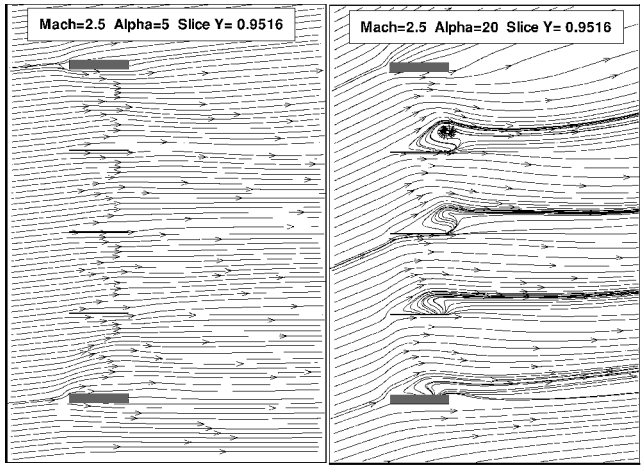

Fig. 21 Streamlines distributions of the horizontal grid-fin X–Z cross section (Y = 0.9516 caliber), Mach number 2.5, 5- and 20-deg angle of attack.

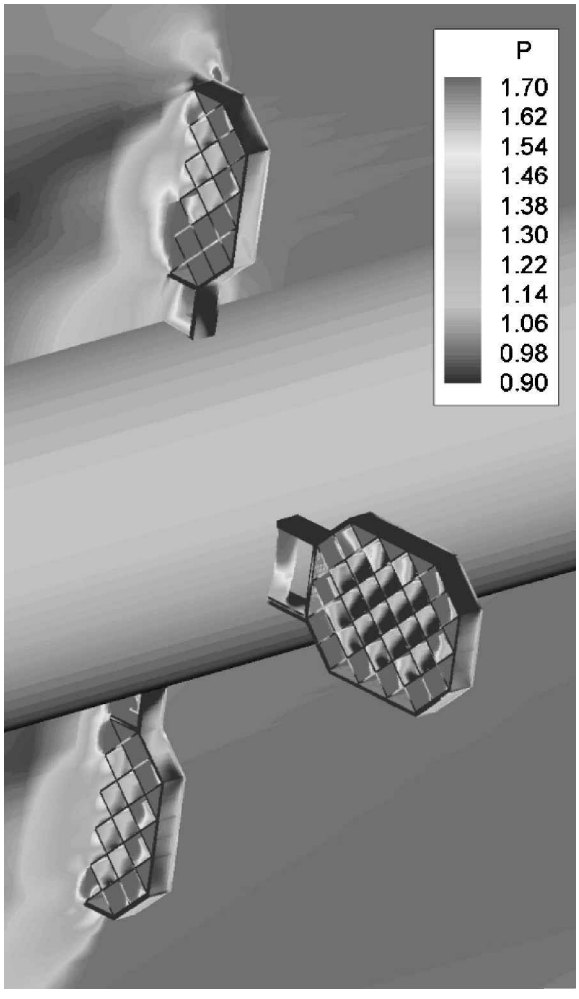

Fig. 22 Surface-pressure distributions of cruciform-fins/body configuration, Mach number 2.5, and 5-deg angle of attack.

fin/body combination, it implies that the differences of each aerodynamic coefficient between planar-form and cruciform-fins/body shape are small, but the total grid number of cruciform-fins/body shape is twice as that of planarform-fins/body shape. Furthermore, the fin-to-fin interference is not significant. Therefore, the computation for the simplified planar-form (i.e., horizontal fin/body) configuration computation is more important for both horizontal fin/body and cruciform configurations.

Conclusions

The specialized grid-generation method combining multiblock and block-off-type grid treatments has been developed for complex grid-fin configuration. The scheme is constructed based on the repeated geometric characteristic, so that three-dimensional fin configuration can be obtained easily after one grid-fin cross-section two-dimensional grid is generated. A similar concept can be applied to generate the horizontal-fin/body shape and cruciform-fin/body shape grid systems. The Navier–Stokes computations provide the detailed flowfields including Mach-number contours, pressure contours, and streamline patterns as well as the integrated aerodynamic coefficients. The computed aerodynamics coefficients of fin with body interference consisting of normal force, bending moment, hinge moment, and axial force that shows different degrees of agreement with the experimental data for different angles of attack and Mach numbers. In general, good agreements are obtained on the normal-force coefficient and the bending-moment coefficient up to larger angles of attack, limited agreements on axial-force coefficient and hinge-moment coefficient except for small angles of attack.

Acknowledgments

We gratefully acknowledge the support of the National Science Council, Taiwan, under Contract NSC89-2213-E-007-071. We also thank the National Center of High Performance Computing, Taiwan, for the use of computer resources.

References

[1]Washington, W. D., and Miller, M. S., "Grid Fins—A New Concept for Missile Stability and Control," AIAA Paper 93-0035, Jan. 1993.

[2]Miller, M. S., and Washington, W. D., "An Experimental Investgation of Grid Fin Drag Reduction Techniques," AIAA Paper 94-1914, Jan. 1994.

[3]Abate, G., Duckerschein, R., and Hathaway, W., "Subsonic/Transonic Free-Flight Tests of a Generic Missile with Grid Fins," AIAA Paper 2000-0937, Jan. 2000.

[4]Burkhalter, J. E., Hartfield, R. J., and Leleux, T. M., "Nonlinear Aerodynamic Analysis of Grid Fin Configurations," *Journal of Aircraft*, Vol. 32, No. 3, 1995, pp. 547–554.

[5]Chen, S., Khalid, M., Xu, H., and Lesage, F., "A Comprehensive CFD Investigation of Grid Fins as Efficient Control Surface Devices," AIAA Paper 2000-0987, Jan. 2000.

[6]DeSpirito, J. Edge, H. L., Weinacht, P., Sahu, J., and Dinavahi, S. P. G., "CFD Analysis of Grid Fins for Maneuvering Missiles," AIAA Paper 2000-0391, Jan. 2000.

[7]DeSpirito, J., Edge, H. L., Weinacht, P., Sahu, J., and Dinavahi, S. P. G., "Viscous CFD Calculations of Grid Fin Missile Aerodynamics in the Supersonic Flow Regime" AIAA Paper 2001-0257, Jan. 2001.

[8]Patankar, S. V., *Numerical Heat Transfer and Fluid Flow*, Hemisphere, Washington, DC, 1980, Chap. 7, pp. 147–149.

[9]Fujii, K., Tamura, Y., and Kuroda, S., "Unified Zonal Method Based on the Fortified Navier–Stokes Concept," AIAA Paper 91-1558, June 1991.

[10]Goldberg, U. C., and Ramakrishnan, S. V., "A Pointwise Version of Baldwin-Barth Turbulence Model," *Computational Fluid Dynamics*, Vol. 1, 1993, pp. 321–328.

[11]Yee, H. C., and Harten, A., "Implicit TVD Schemes for Hyperbolic Conservation Laws in Curvilinear Coordinate," *AIAA Journal* Vol. 25, No. 2, 1987, pp. 266–274.

[12]MacCormack, R. W., "Current Status of Numerical Solutions of the Navier–Stokes Equations," AIAA Paper 85-0032, Jan. 1985.

[13]Coakley, T. J., "Turbulence Modeling Methods for the Compressible Navier–Stokes Equations," AIAA Paper 83-1693, July 1983.

[14]Siikonen, T., "An Application of Roe's Flux-Difference Splitting for k-ε Turbulence Model," *International Journal for Numerical Methods in Fluids*, Vol. 21, 1995, pp. 1017–1039.

[15]Shuen, Jian-Shun, "Upwind Differencing and LU Factorization for Chemical Non-Equilibrium Navier–Stokes Equations," *Journal of Computational Physics*, Vol. 40, No. 2, 1981, pp. 233–250.

[16]Pulliam, T. H., and Steger, J. L., "Recent Improvements in Efficient, Accuracy, and Convergence for Implicit Approximate Factorization Algorithms," AIAA Paper 85-0360, Jan. 1985.

[17]Gordon, W. J., and Hall, C. A., "Construction of Curvilinear Coordinates Systems and Applications to Mesh Generation," *International Journal for Numerical Methods in Engineering*, Vol. 7, 1973, pp. 761–777.

W. E. Williamson
Associate Editor